Chinese Journal of Aeronautics, (2017), 30(3): 1217–1230

Chinese Society of Aeronautics and Astronautics
& Beihang University

Chinese Journal of Aeronautics

cja@buaa.edu.cn
www.sciencedirect.com

Beam-pointing error compensation method of phased array radar seeker with phantom-bit technology

Qiuqiu WEN [a,*], **Tianyu LU** [b], **Qunli XIA** [a], **Zedong SUN** [c]

[a] *School of Aerospace Engineering, Beijing Institute of Technology, Beijing 100081, China*
[b] *Beijing Aerospace Automatic Control Institute, Beijing 100854, China*
[c] *Army Aviation Institute, Beijing 100041, China*

Received 29 June 2016; revised 8 October 2016; accepted 21 December 2016
Available online 8 May 2017

KEYWORDS

Beam-pointing error;
Beam scanning control;
Line-of-sight rate extraction;
Phantom-bit technology;
Phased array radar seeker

Abstract A phased array radar seeker (PARS) must be able to effectively decouple body motion and accurately extract the line-of-sight (LOS) rate for target missile tracking. In this study, the real-time two-channel beam pointing error (BPE) compensation method of PARS for LOS rate extraction is designed. The PARS discrete beam motion principium is analyzed, and the mathematical model of beam scanning control is finished. According to the principle of the antenna element shift phase, both the antenna element shift phase law and the causes of beam-pointing error under phantom-bit conditions are analyzed, and the effect of BPE caused by phantom-bit technology (PBT) on the extraction accuracy of the LOS rate is examined. A compensation method is given, which includes coordinate transforms, beam angle margin compensation, and detector dislocation angle calculation. When the method is used, the beam angle margin in the pitch and yaw directions is calculated to reduce the effect of the missile body disturbance and to improve LOS rate extraction precision by compensating for the detector dislocation angle. The simulation results validate the proposed method.

1. Introduction

The phased array radar seeker (PARS) is a new type of guidance system with many advantages, such as rapidity, flexibility, high range, and strong anti-jamming capability, making it of interest for upgrading the homing guidance missile systems.[1,2] Different with traditional mechanical scanning radar seekers, PARS is strapped on the missile body and conducts beam scanning via the phase shift value of the elements radiating from the digital phase shifter.[3] But the beam granularity

* Corresponding author.
E-mail address: wenqiuqiu82@bit.edu.cn (Q. WEN).

Peer review under responsibility of Editorial Committee of CJA.

ELSEVIER Production and hosting by Elsevier

http://dx.doi.org/10.1016/j.cja.2017.03.020
1000-9361 © 2017 Chinese Society of Aeronautics and Astronautics. Production and hosting by Elsevier Ltd.

appears during the beam scanning process, causing the beam to scan discretely and reducing PARS beam scanning accuracy.[4–6] In order to control beam granularity, the phantom-bit technology (PBT) has been widely applied in PARS. Although the PBT can improve the PARS beam scanning accuracy, it also negatively affects the beam pointing error, which will lead to body movement incompletely decoupling when the beam pointing and inertial measurement unit information are used to extract the guidance information.[7–9]

Furthermore, as a target detection device, PARS should output the line-of-sight (LOS) rate for the guidance of a homing missile by using the proportional navigation law.[10] Obtaining of LOS of PARS is calculated from inertial measurements of missile attitude angle and beam angle.[11] The beam pointing error will lead to wrong LOS rate output, and then decrease guidance performance. Thereby, studying beam-pointing error caused by PBT is of important significance to calibration of PARS as well as stability and accuracy of guidance system.

In Refs. 12,13, some scholars have studied problems caused by quantization error of PARS and corresponding solutions. But the above references only consider the lack of an initial antenna scanning angle, which prevents the array antenna elements within the sub-array from scanning. Moreover, in Ref. 14, the problem caused by pointing error of strap-down phased array seeker applied in satellite communication was studied. However, there are few research studies on the guidance problem caused by PBT and related solution strategies.

Similar with PBT, the radome boresight error of PARS can also affect the output of LOS rate. It would induce a disturbance rejection rate that would result in a disturbance rejection rate parasitical loop in the guidance loop. In Refs. 15,16, the effects of the radar seeker radome boresight error on the stability and guidance accuracy of homing missiles were investigated. In Refs. 17,18, the effect of the disturbance rejection rate caused by spring torque and damping torque on the stability of the guidance system was analyzed. At the same time, Janice et al.[2] stated that radome boresight error is a key technique to be urgently solved for the terminal guidance of homing missiles. Peterson et al.[19] proposed a type of radome boresight error compensation method. The related results and methods are useful for this study.

The current study aims to present a real-time two-channel beam-pointing error compensation method for PARS LOS rate extraction. To this end, the PARS discrete beam motion principium is given firstly. According to the principle of the antenna element shift phase, the mathematical model of beam scanning control is built. Both the antenna element shift phase law and the causes of beam-pointing error under phantom-bit conditions are analyzed. Furthermore, the effect of BPE caused by PBT on the extraction accuracy of the LOS rate and stability margin of the guidance system is examined. Then, a two-channel LOS rate extraction model using a beam-pointing error compensation method, which includes coordinate transforms, beam angle margin compensation, and detector dislocation angle calculation, is proposed. Finally, results of numerical simulations for four conditions are presented, and the effectiveness of the compensation method is proved.

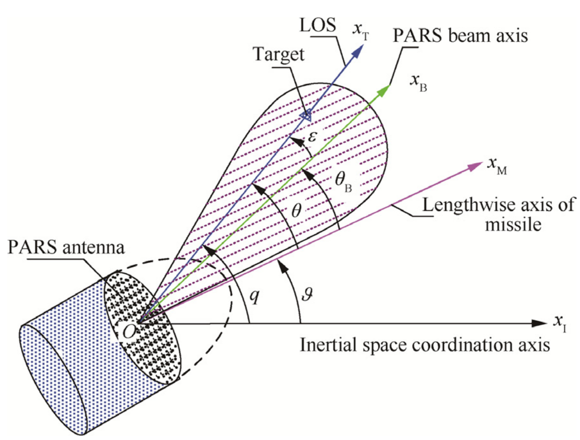

Fig. 1 Engagement geometry between missile and target.

2. PARS beam control and beam-pointing error

2.1. Target tracking control and LOS rate output principle

The relative position relationship of the PARS beam, missile, and target in a portrait plane is shown in Fig. 1. The missile center of mass is defined as point O, the inertial space coordinate axis is defined as Ox_I, and the lengthwise axis of the missile is expressed as Ox_M. Ox_B is the PARS beam axis, and Ox_T is the direction to the target. In Fig. 1, ϑ is the body attitude angle, q the LOS angle, θ the angle between the LOS and the lengthwise axis of the missile, θ_B the beam direction angle, and ε the detector dislocation angle.

The target tracking control loop diagram of PARS is shown in Fig. 2. Here, $\dot{q}$ is the true LOS rate, $\dot{\vartheta}_{IMU}$ the angular velocity of the body measured by the inertial measurement unit (IMU) on the missile, k the control gain, $G_\varepsilon(s)$ the dynamics of PARS's monopulse angle measurement, $G_{IMU}(s)$ the

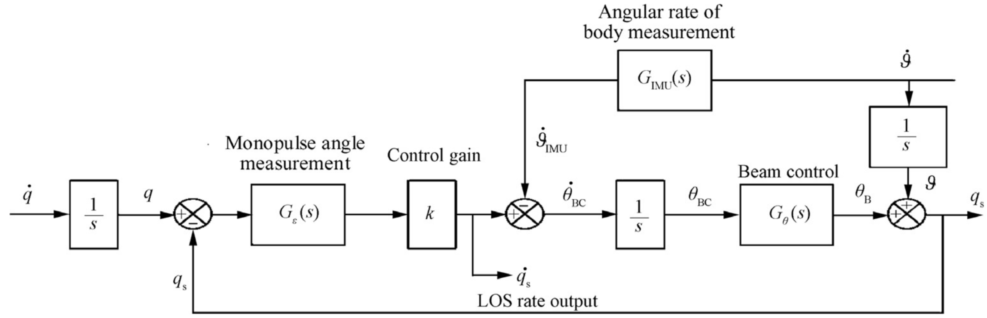

Fig. 2 Target tracking control loop of PARS.

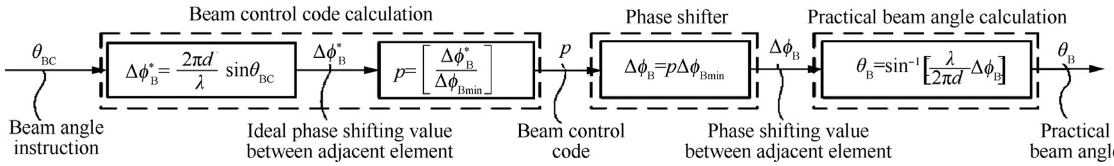

Fig. 3 Beam control principle diagram of PARS.

dynamics of PARS's angular rate of body measurement, and $G_\theta(s)$ the beam control measurement.

According to Fig. 3, the beam angle control command can be written as

$$\theta_{BC} = \int (\varepsilon_s k + \dot{\vartheta}_{IMU}) \tag{1}$$

where ε_s is the dislocation angle measured by PARS.

And the LOS rate output of PARS is

$$\dot{q}_s = \dot{q}\frac{\frac{1}{G_\theta(s)}}{\frac{s}{G_\varepsilon(s)G_\theta(s)k}+1} + \dot{\vartheta}\left(\frac{G_{IMU}(s)}{\frac{s}{G_\varepsilon(s)G_\theta(s)k}+1} - \frac{\frac{1}{G_\theta(s)}}{\frac{s}{G_\varepsilon(s)G_\theta(s)k}+1}\right) \tag{2}$$

In this study, the dynamics of PARS's monopulse angle measurement and IMU are assumed to be fast enough. Thereby, Eq. (2) is simplified via $G_\varepsilon(s) = G_{IMU}(s) = 1$

$$\dot{q}_s = \dot{q}_s^{Los} + \dot{q}_s^{\dot{\vartheta}} \tag{3}$$

$$\dot{q}_s^{Los} = \dot{q}\frac{k}{s + G_\theta(s)k} \tag{4}$$

$$\dot{q}_s^{\dot{\vartheta}} = \dot{\vartheta}\frac{(G_\theta(s)-1)k}{s + G_\theta(s)k} \tag{5}$$

where $\dot{q}_s^{Los}$ presents the LOS rate output from the true LOS rate variation and $\dot{q}_s^{\dot{\vartheta}}$ the LOS rate output caused by the body angular velocity.

Eq. (5) shows that the disturbance rejection rate caused by body movement will be zero when the beam control $G_\theta(s)$ equals one. If not, the body movement ($\dot{\vartheta}$) will be coupled into the LOS rate output of PARS. As a result, the performance of the PARS beam control becomes the key for decoupling body movement from the LOS rate.

2.2. PARS beam control

When the radiating element phase shift value of PARS is $\Delta\phi_B$, the element spacing is d, the radar wavelength is λ, and the angle (θ_B) of the beam-pointing deviation from the normal direction of the antenna is certain, which can be expressed as follows:

$$\theta_B = \sin^{-1}(\lambda\Delta\phi_B/2\pi d) \tag{6}$$

We can determine from Eq. (6) that the antenna direction changes with changing phase shift value, and $\Delta\phi_B$ is obtained from the digital phase shifter. When the digit of the phase shifter is K (K is a positive integer), the minimum phase shift value can be expressed as follows:

$$\Delta\phi_{Bmin} = 2\pi/2^K \tag{7}$$

The radiating element phase shift value from the phase shifter is expressed as follows:

$$\Delta\phi_B = p\Delta\phi_{Bmin} \tag{8}$$

where p is the beam control code, which is provided by the digital phase shifter, $p = 0, 1, 2, \ldots, 2^K - 1$. Notice that $\Delta\phi_B$ is discrete from Eq. (8), and then the beam movement is also discrete according to Eq. (6). As a result, PARS broadcasts electromagnetic waves based on the beam angle instruction (θ_{BC}), when a missile tracks a target.

Fig. 3 shows the beam control principle diagram of PARS. We can obtain the ideal phase shift value ($\Delta\phi^*_B$) between the adjacent elements on the basis of the beam angle instruction (θ_{BC}). The beam control code (p) can be obtained by rounding $\Delta\phi^*_B/\Delta\phi_{Bmin}$. The phase shifter output practical phase shift value ($\Delta\phi_B = p\Delta\phi_{Bmin}$) between adjacent elements is obtained according to p. The practical beam angle (θ_B) can be obtained by Eq. (3).

2.3. Phantom-bit technology

Beam granularity ($\theta_{B(p+1)} - \theta_{B(p)}$) is determined by the bit of the phase shifter. A smaller bit leads to larger beam granularity. To reduce beam granularity and make the phased array antenna scanning approach the level of mechanical continuous scanning, the bit should be increased. With the cost and complexity considered, the PBT is widely applicable in practical engineering. With PBT, PARS could achieve performance approximate to that of a high-bit phase shifter by using a low-bit phase shifter. Fig. 4 shows the principle architecture of the PBT phase shift. The control signal register and arithmetic unit correspond to a high-bit phase shift. The low m-bit binary codes of the arithmetic unit are eliminated during phase shifter setting, while high-bit binary codes are sent to the phase shifter to finish unit phase setting.[3] If the actual bit of the phase shifter is b and the phantom bit is m, the phase control computer will calculate the minimum phase shift value ($\Delta\phi_{Bmin} = 2\pi/2^K$) with $K = b + m$ bits. The beam control code p is expressed by a binary figure in the control signal register

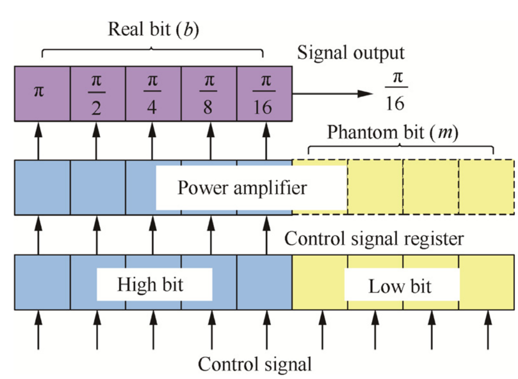

Fig. 4 Principle of phase shift for PBT.

and arithmetic unit, and the theoretical phase shift code is expressed as $Z = ip$ for element No. i; with the low m-bit eliminated, we set $Z - \mathrm{mod}\,(Z, 2^m)$ as the practical phase shift code, where $\mathrm{mod}\,(Z, 2^m)$ is the remainder when Z is divided by 2^m.

This study used a missile diameter of 120 mm, and Ka waveband (8 mm wavelength) is used to meet the ratio of the element spacing to radar wavelength $d/\lambda = 0.5$. The number of antenna elements N is usually 30, but we set N to 32 for convenience. The phase shifter adopts the PBT ($b = 5$, $m = 4$). Fig. 5 shows the practical phase shift value with PBT when the beam control code p is from 1 to 2^m (2^m is one period). This shows that the number of the sub-array will increase as the beam control code increases, while the phase shift value is identical in every sub-array.

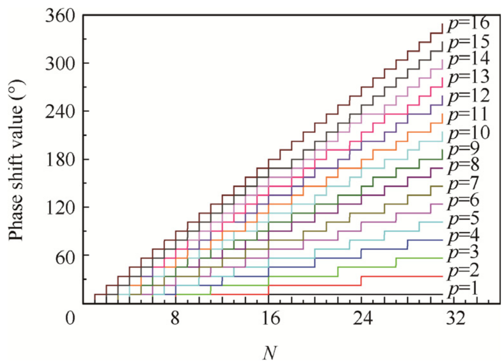

Fig. 5 Unit phase shift value used for PBT.

2.4. BPE and BPES

The variation law of the phase shift error when the beam control code changes from $p = 1$ to $p = 2^m$ was analyzed by the end-off approach.[3] Fig. 6 shows the results, and we can easily see that the phase shift errors are centered at the 8th phantom-bit jump in one period, presenting an anti-symmetric distribution pattern.

The phase shift error causes differences between virtual beam pointing and theoretical beam pointing. This indicates the positive correlation between the BPE distribution law and phase shift error distribution law. BPE distributions under different phantom bits ($m = 3$, $m = 4$ and $m = 5$) but fixed $N = 32$ and $b = 5$ are shown in Fig. 7.

From Fig. 7, we can easily see that BPE changes periodically (2^m is one period). It presents an anti-symmetric distribution centered on the central jump of the phantom-bit period. The BPE envelope line will increase with the increase of the beam control code and phantom bits, respectively.

If Δ denotes the angle between the theoretical beam angle (θ_{BC}) and practical beam angle (θ_{B}) in one phantom-bit period caused by the BPES, we have

$$\theta_{\mathrm{B}} = \theta_{\mathrm{BC}} + \Delta \tag{9}$$

Differentiation of Eq. (6) yields

$$\dot{\theta}_{\mathrm{B}} = (1 + R_i)\dot{\theta}_{\mathrm{BC}} \tag{10}$$

where $R_i = \partial\Delta/\partial\theta_{\mathrm{BC}}$ present the effects of BPES on the beam angle control and i the numbers of phantom bits, which correspond to $m = 3$, 4 and 5. In practical engineering applications, BPES can be eliminated via calibration technology; to lighten the calibration workload, usually every one phantom-bit

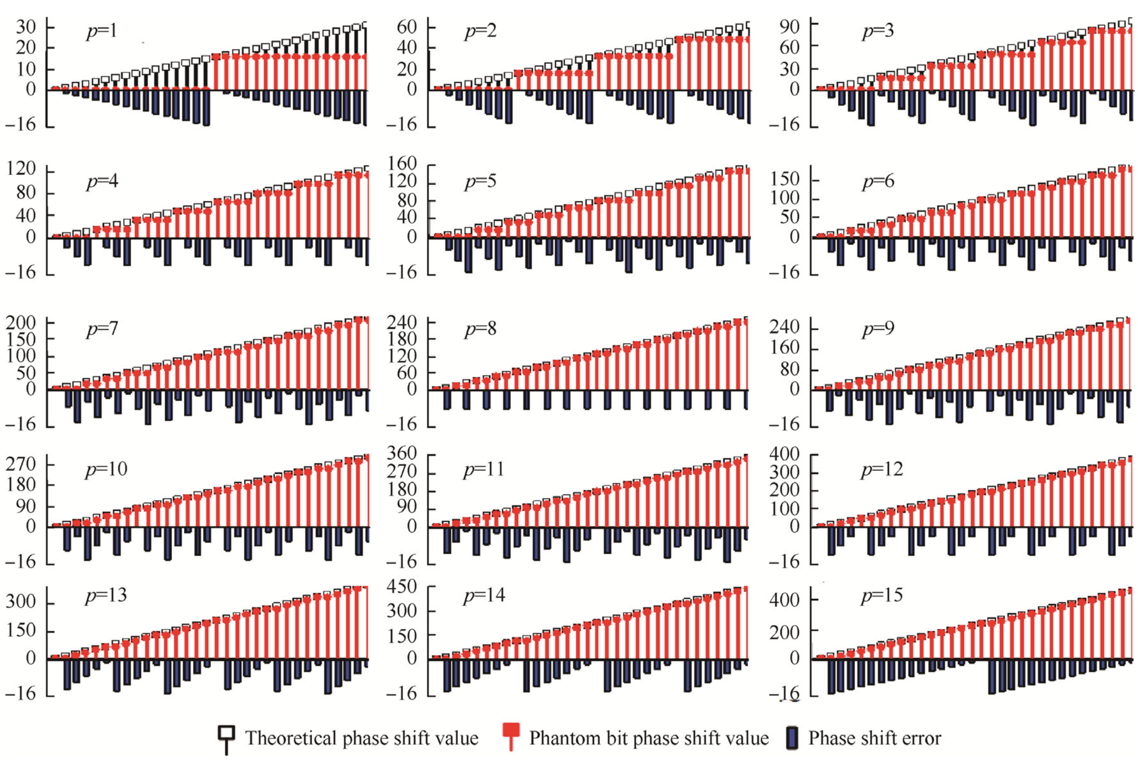

Fig. 6 Phase shift distribution law.

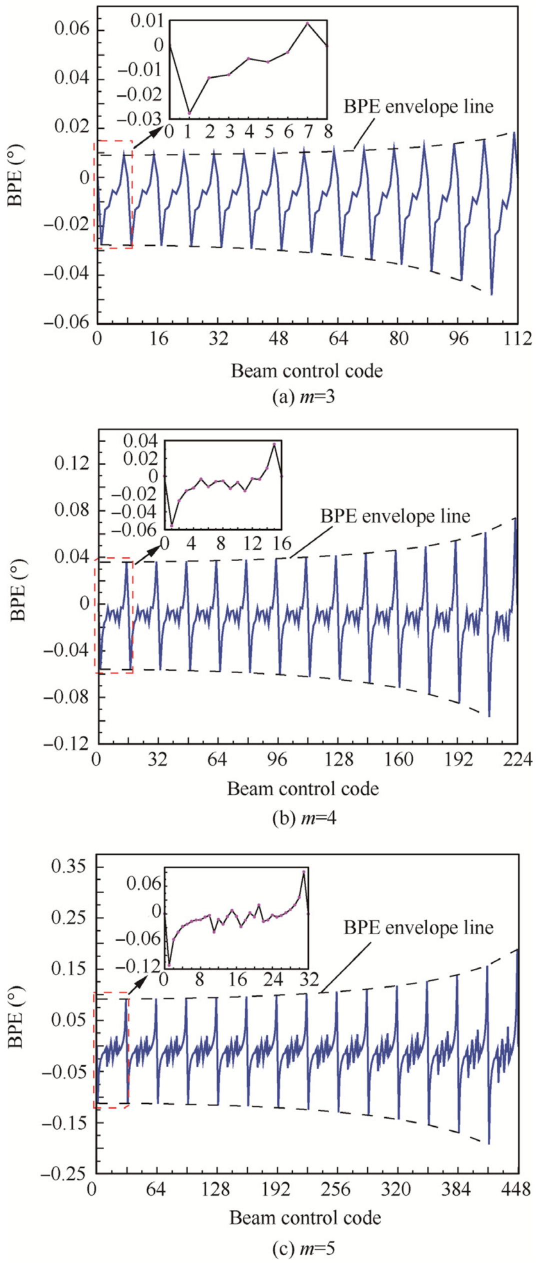

Fig. 7 BPE caused by PBT.

period ($\Delta\theta_{BC} = 3.58°$) is calibrated. As shown in Table 1, the maximum BPES can be expressed as $R_3 \approx \pm 0.01$, $R_4 \approx \pm 0.03$ and $R_5 \approx \pm 0.05$.

According to Eq. (10), $G_\theta(s)$ in Eqs. (3)–(5) can be expressed as $G_\theta(s) = 1 + R_i$. Then, the PARS's LOS rate output is

$$\dot{q}_s = \dot{q}\frac{k}{s + (1 + R_i)k} + \dot{\vartheta}\frac{(1 + R_i)k - 1}{s + (1 + R_i)k} \tag{11}$$

and

$$\dot{q}_s^{Los} = \dot{q}\frac{k}{s + G_\theta(s)k} \tag{12}$$

$$\dot{q}_s^{\vartheta} = \dot{\vartheta}\frac{(G_\theta(s) - 1)k}{s + G_\theta(s)k} \tag{13}$$

Table 1 Variation of BPE with different phantom bits.

Phantom bit	Positive beam-pointing error (°)	Negative beam-pointing error (°)
m = 3	$\Delta = 0.03665$	$\Delta = -0.03865$
m = 4	$\Delta = 0.10943$	$\Delta = -0.11543$
m = 5	$\Delta = 0.18819$	$\Delta = -0.190191$

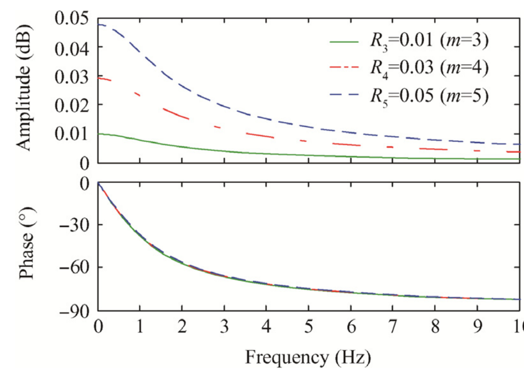

Fig. 8 Line-of-sight rate output Bode diagrams regarding different phantom-bit numbers.

From Eq. (13), it can be found that the LOS rate output $\dot{q}_s^{\vartheta}$ caused by the angular missile body is not equal to zero unless R_i is equal to zero. According to the Bode diagram of the LOS angle rate under different PBNs, presented in Fig. 8, the disturbance of the missile body will lead to additional line-of-sight angle-rate output. The greater the virtual digit is, the larger the amplitude of the additional line-of-sight angle-rate output will be. However, the virtual digit hardly affects the phase characteristics.

2.5. Effect on guidance loop

To analyze the influence of BPES on the guidance loop, a closed guidance loop for a perfectly stabilized PARS, along with BPES interactions, is given in Fig. 9. Here, a fourth-order binomial representation of the missile homing guidance, including a first-order model for a noise filter and third-order model for the control system, is used. Let $G_\varepsilon(s) = G_{IMU}(s) = 1$, and the guidance transfer function is

$$\frac{a_m}{\dot{q}} = \frac{eV_c}{\left(\frac{1}{k}s + 1 + R\right)\left(\frac{T_g}{4}s + 1\right)^4 - \frac{eRV_c}{V_m}(T_\alpha s + 1)} \tag{14}$$

where e is the effective navigation ratio, V_c the closing velocity, V_m the flight speed of the missile, T_g the guidance time constant, T_α the time constant of the angle of attack, and a_m the missile acceleration.

According to Table. 1, $|R| \ll 1$, and then Eq. (12) can be simplified as

$$\frac{a_m}{\dot{q}} = \frac{eV_c}{\left(\frac{1}{k}s + 1\right)\left(\frac{T_g}{4}s + 1\right)^4 - \frac{eRV_c}{V_m}(T_\alpha s + 1)} \tag{15}$$

The guidance system characteristic equation is

$$\Phi(s) = \left(\frac{1}{k}s+1\right)\left(\frac{T_g}{4}s+1\right)^4 - \frac{eRV_c}{V_m}(T_\alpha s+1) = 0 \quad (16)$$

The guidance system transfer function is stable only if the poles of Eq. (16) are in the left-half plane. If the normalization factors:

$$\begin{cases} \bar{s} = T_g s \\ \overline{T}_\alpha = T_\alpha / T_g \\ T_k = 1/k \\ \overline{T}_k = T_k / T_g \\ \overline{R} = e(V_c/V_m)R \end{cases}$$

are used, Eq. (16) becomes

$$\Phi(s) = \frac{\overline{T}_k}{256}\bar{s}^5 + \left(\frac{\overline{T}_k}{16}+\frac{1}{256}\right)\bar{s}^4 + \left(\frac{3\overline{T}_k}{8}+\frac{1}{16}\right)\bar{s}^3 + \left(\overline{T}_k+\frac{3}{8}\right)\bar{s}^2 + (\overline{T}_k - \overline{R}\,\overline{T}_\alpha + 1)\bar{s} + (1-\overline{R}) \quad (17)$$

The coefficients of Eq. (17) are defined as

$$\begin{cases} B_0 = (1-\overline{R}) \\ B_1 = (\overline{T}_k - \overline{R}\overline{T}_\alpha + 1) \\ B_2 = (\overline{T}_k + \frac{3}{8}) \\ B_3 = \left(\frac{3\overline{T}_k}{8} + \frac{1}{16}\right) \\ B_4 = \left(\frac{\overline{T}_k}{16} + \frac{1}{256}\right) \\ B_5 = \frac{\overline{T}_k}{256} \end{cases} \quad (18)$$

The Routh criterion guarantees stability of the guidance system transfer function if the coefficients of Eq. (18) are positive ($B_0, B_1, \ldots, B_5 > 0$) and if the following additional quantities are positive:

$$\begin{cases} a_1 = \frac{B_4B_3 - B_5B_2}{B_4} \\ b_1 = \frac{a_1B_2 - B_4a_2}{a_1} \\ c_1 = \frac{b_1a_2 - a_1b_2}{b_1} \\ d_1 = b_2 \end{cases} \quad (19)$$

where

$$a_2 = \frac{B_4B_1 - B_5B_0}{B_4}, \quad b_2 = B_0 \quad (20)$$

The stability of the guidance system transfer function is determined numerically for all values of the ratio $\overline{T}_\alpha$, $\bar{R}$ and the parameter $\overline{T}_k$, and the results are plotted in Fig. 10.

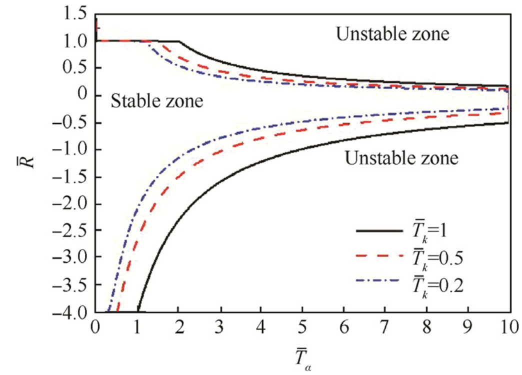

Fig. 10 Stability range of guidance system transfer function.

Clearly, larger values of $|\bar{R}|$ lead to a smaller range of stability for $\overline{T}_\alpha$, and small values of $|\bar{R}|$ give the widest possible range of stability. Thereby, it is necessary to control BPES for a large stability margin.

3. Decoupling algorithm of two channels used in BPE compensation

3.1. BPE compensation principle

The above analysis shows that, when R is equal to zero, the practical beam angle (θ_B) is equal to the beam angle instruction (θ_{BC}), and PARS tracking loop can decouple body movement completely. Due to the beam control link, which uses PBT, the practical beam angle (θ_B) is not equal to the beam angle instruction (θ_{BC}); then, body movement is coupled with the LOS rate output, and the disturbance rejection rate parasitic loop will be introduced into the guidance loop of the missile, which affects the target-tracking performance of the missile. Furthermore, R is not constant, which will cause volatility of the detector dislocation angle. The key cause of the above phenomenon is that R is not equal to zero. According to Fig. 3, we design a compensation loop to eliminate the effect of the beam control link. Fig. 11 shows the BPE compensation principle diagram.

In Fig. 11, θ_{BC} is measurable, θ_B can be obtained by beam control code, and thus BPE (Δ) can be calculated by θ_{BC} minus θ_B in real time.

The PARS tracking loop transfer function can be expressed based on the simplified model using BPE compensation.

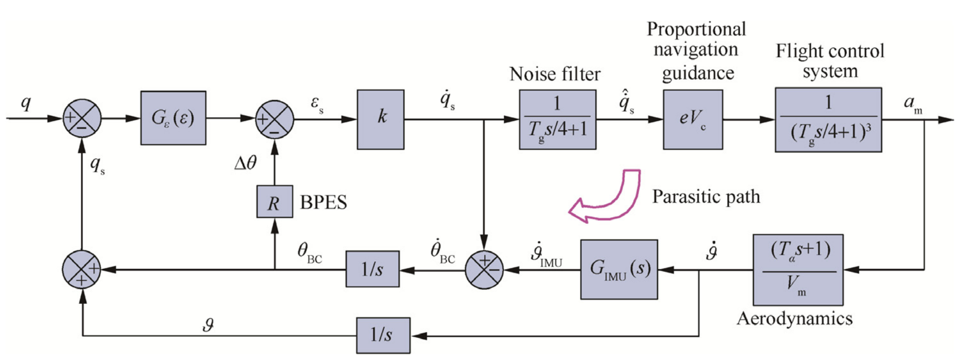

Fig. 9 Diagram of guidance loop with BPES.

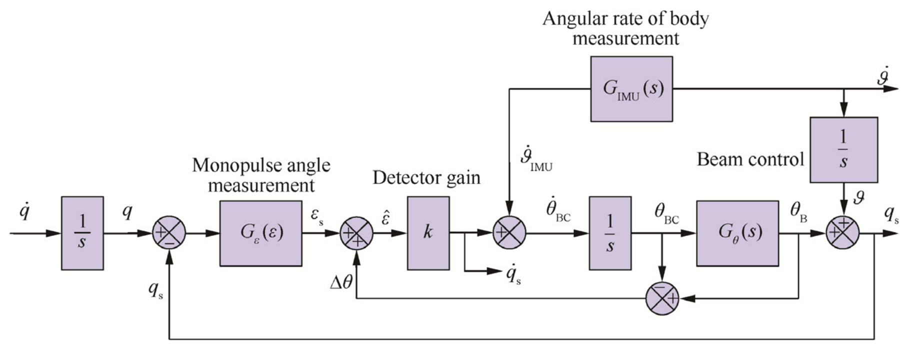

Fig. 11 BPE compensation principle diagram.

$$\dot{q}_s = \frac{k_s}{s + k_s}\dot{q} \tag{21}$$

A comparison of Eqs. (11) and (21) shows that the effect of the body movement can be eliminated completely after BPE compensation is used, and the beam volatility is also resolved. At the same time, the PARS tracking loop transfer function is described as a first-order process of the phase lag.

3.2. Beam angle margin calculation

For the relationship between S_b and $S_{\hat{b}}$, the beam angle margin of PARS is applied in the 3D space. Fig. 12 shows the angle relationship between S_b and $S_{\hat{b}}$. The related coordinate system and the angle definition are given in Appendix A.

The beam angle instructions (θ_{BCy}, θ_{BCz}) can be obtained via the measurement value of S_b at time t, and the practical beam angle (θ_{By}, θ_{Bz}) can be obtained via the beam control model and the calibration technique. The unit vector in $S_{\hat{b}}$ is presumably $\boldsymbol{a}^{\hat{b}} = [1, 0, 0]^T$, which can be projected to S_b at time t, denoted as $\boldsymbol{a}^b$. The transformational matrix about the coordinate system is denoted as $\boldsymbol{C}$. The subscript indicates the transformational direction, for example, $\boldsymbol{C}_{mb}$ denotes the transformational matrix from S_m to S_b. Thereafter,

$$\boldsymbol{a}^b = \boldsymbol{C}_{b\hat{b}}\boldsymbol{a}^{\hat{b}} = \boldsymbol{C}_{mb}(\theta_{BCy}, \theta_{BCz})\boldsymbol{C}_{\hat{b}m}(\theta_{By}, \theta_{Bz})\boldsymbol{a}^{\hat{b}} \tag{22}$$

where

$$\boldsymbol{C}_{\hat{b}m} = \boldsymbol{C}_{m\hat{b}}^{-1} = \begin{bmatrix} \cos\theta_{By}\cos\theta_{Bz} & \sin\theta_{Bz} & -\sin\theta_{By}\cos\theta_{Bz} \\ -\cos\theta_{By}\sin\theta_{Bz} & \cos\theta_{Bz} & \sin\theta_{By}\sin\theta_{Bz} \\ \sin\theta_{By} & 0 & \cos\theta_{By} \end{bmatrix}$$

$$\boldsymbol{C}_{mb} = \begin{bmatrix} \cos\theta_{BCy}\cos\theta_{BCz} & \sin\theta_{BCz} & -\sin\theta_{BCy}\cos\theta_{BCz} \\ -\cos\theta_{BCy}\sin\theta_{BCz} & \cos\theta_{BCz} & \sin\theta_{BCy}\sin\theta_{BCz} \\ \sin\theta_{BCy} & 0 & \cos\theta_{BCy} \end{bmatrix}$$

$\boldsymbol{C}_{\hat{b}m}$ and $\boldsymbol{C}_{mb}$ are then substituted into Eq. (6). $\boldsymbol{a}^b$ is then obtained at time t. We suppose that $\boldsymbol{a}^b = [a_x^b, a_y^b, a_z^b]^T$, given that the maximum beam control error is 0.3°. $\Delta\theta_y$ and $\Delta\theta_z$ are small. Thus, $\Delta\theta_y$ and $\Delta\theta_z$ are expressed as follows:

$$\begin{cases} \Delta\theta_y = \arctan\left(-\frac{a_z^b}{a_x^b}\right) \\ \Delta\theta_z = \arctan\left(-\frac{a_y^b}{a_x^b}\right) \end{cases}$$

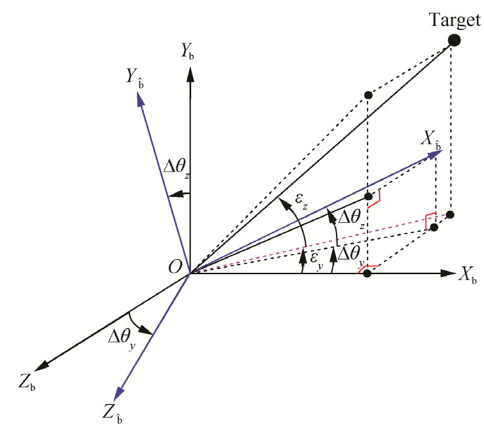

Fig. 12 Angle relationship between S_b and $S_{\hat{b}}$.

3.3. Beam angle control commands

The PARS dislocation angle is the angular deviation between the beam-pointing coordinate system x_b-axis and LOS coordinate system x_l-axis in the pitch and yaw directions. Beam-pointing coordinate systems on the y_b-axis and z_b-axis are considered real-time rotation axes. The beam control model causes the beam-pointing center (ox_b) to rotate at an angular rate ($\dot{q}_{sy}$, $\dot{q}_{sz}$) proportional to the actual detector dislocation angle ($\hat{\varepsilon}_y$, $\hat{\varepsilon}_z$). Given that LOS motion is a slow variable and beam scanning motion is a fast variable, the detector dislocation angle can be eventually eliminated by closed-loop tracking. Thus, fast tracking of the target is realized.

The rotation angular rate of the beam-pointing axis relative to the inertial space can be expressed as follows:

$$\begin{cases} \dot{q}_{sy} = k\hat{\varepsilon}_y \\ \dot{q}_{sz} = k\hat{\varepsilon}_z \end{cases} \tag{23}$$

Beam motion in the inertial space is composed of two parts. One is the motion of the beam-pointing axis relative to the missile body, whereas the other is the motion of the missile body relative to the inertial space. Thus, the mathematical expression is as follows:

$$\boldsymbol{\omega}_{bi}^I = \boldsymbol{\omega}_{bm}^I + \boldsymbol{\omega}_{mi}^I \tag{24}$$

where $\boldsymbol{\omega}$ is the rotation angular rate vector; the subscripts denote the coordinate system transformational relation, and the superscript denotes the vector projection coordinate system. For example, $\boldsymbol{\omega}_{\mathrm{bi}}^{\mathrm{B}}$ denotes the rotation angular rate projection of the beam-pointing axis relative to the inertial space in the beam-pointing coordinate system.

According to Eq. (24), the following is obtained by multiplying both sides by the coordinate transformational matrix ($\boldsymbol{C}_{\mathrm{ib}}$):

$$\boldsymbol{C}_{\mathrm{ib}}\boldsymbol{\omega}_{\mathrm{bi}}^{\mathrm{I}} = \boldsymbol{C}_{\mathrm{ib}}\boldsymbol{\omega}_{\mathrm{bm}}^{\mathrm{I}} + \boldsymbol{C}_{\mathrm{ib}}\boldsymbol{\omega}_{\mathrm{mi}}^{\mathrm{I}}$$

where $\boldsymbol{C}_{\mathrm{ib}}$ denotes the transformational matrix from S_i to S_b. The equation can be rewritten as follows:

$$\boldsymbol{\omega}_{\mathrm{bi}}^{\mathrm{B}} = \boldsymbol{\omega}_{\mathrm{bm}}^{\mathrm{B}} + \boldsymbol{\omega}_{\mathrm{mi}}^{\mathrm{B}} \tag{25}$$

where

$$\boldsymbol{\omega}_{\mathrm{bm}}^{\mathrm{B}} = \boldsymbol{C}_{\mathrm{mb}}\begin{bmatrix} 0 \\ \dot{\theta}_{\mathrm{BC}y} \\ 0 \end{bmatrix} + \begin{bmatrix} 0 \\ 0 \\ \dot{\theta}_{\mathrm{BC}z} \end{bmatrix} = \begin{bmatrix} \dot{\theta}_{\mathrm{BC}y}\sin\theta_{\mathrm{BC}z} \\ \dot{\theta}_{\mathrm{BC}y}\cos\theta_{\mathrm{BC}z} \\ \dot{\theta}_{\mathrm{BC}z} \end{bmatrix} \tag{26}$$

$[\omega_x, \omega_y, \omega_z]^{\mathrm{T}}$ denotes the rotation angular rate projection of the missile body relative to the inertial space in the missile body coordinate system, which can be measured by the gyroscope rate on the body. In Eq. (17),

$$\boldsymbol{\omega}_{\mathrm{mi}}^{\mathrm{B}} = \begin{bmatrix} \omega_x\cos\theta_{\mathrm{BC}y}\cos\theta_{\mathrm{BC}z} + \omega_y\sin\theta_{\mathrm{BC}z} - \omega_z\sin\theta_{\mathrm{BC}y}\cos\theta_{\mathrm{BC}z} \\ -\omega_x\cos\theta_{\mathrm{BC}y}\sin\theta_{\mathrm{BC}z} + \omega_y\cos\theta_{\mathrm{BC}z} + \omega_z\sin\theta_{\mathrm{BC}y}\sin\theta_{\mathrm{BC}z} \\ \omega_x\sin\theta_{\mathrm{BC}y} + \omega_z\cos\theta_{\mathrm{BC}y} \end{bmatrix} \tag{27}$$

$\boldsymbol{\omega}_{\mathrm{mi}}^{\mathrm{B}}$ is expressed as $[\omega_{\mathrm{b}x}, \omega_{\mathrm{b}y}, \omega_{\mathrm{b}z}]^{\mathrm{T}}$. The combination of Eqs. (25)–(27) can be rewritten as follows:

$$\boldsymbol{\omega}_{\mathrm{bi}}^{\mathrm{B}} = \begin{bmatrix} \dot{\theta}_{\mathrm{BC}y}\sin\theta_{\mathrm{BC}z} + \omega_{\mathrm{b}x} \\ \dot{\theta}_{\mathrm{BC}y}\cos\theta_{\mathrm{BC}z} + \omega_{\mathrm{b}y} \\ \dot{\theta}_{\mathrm{BC}z} + \omega_{\mathrm{b}z} \end{bmatrix} \tag{28}$$

PARS only outputs the LOS rate in the pitch and yaw directions. Eq. (28) is equivalent to the following:

$$\begin{cases} \dot{q}_{\mathrm{s}y} = \dot{\theta}_{\mathrm{BC}y}\cos\theta_{\mathrm{BC}z} + \omega_{\mathrm{b}y} \\ \dot{q}_{\mathrm{s}z} = \dot{\theta}_{\mathrm{BC}z} + \omega_{\mathrm{b}z} \end{cases} \tag{29}$$

The beam rotation angular rate of the beam-pointing axis relative to the missile body can be calculated by Eq. (29):

$$\begin{cases} \dot{\theta}_{\mathrm{BC}y} = (\dot{q}_{\mathrm{s}y} - \omega_{\mathrm{b}y})/\cos\theta_{\mathrm{BC}z} \\ \dot{\theta}_{\mathrm{BC}z} = \dot{q}_{\mathrm{s}z} - \omega_{\mathrm{b}z} \end{cases} \tag{30}$$

On the basis of the integral operation, we can obtain the beam control instructions $\theta_{\mathrm{BC}y}$ and $\theta_{\mathrm{BC}z}$ in the pitch and yaw directions, respectively.

Fig. 13 shows the LOS rate extraction model for the two channels by BPE compensation. The model includes the detector dislocation angle calculation model, beam angle margin calculation model, and discrete beam control model. Each parameter has been given in the previous model building.

4. Simulation analysis

In this section, the tracking performance of PARS is verified through various simulations. First, we considered the discrete beam control model (Fig. 4) to test the results of BPT compensation at different disturbance frequencies of the missile. The actual bit of the digital phase shifter is set as $b = 5$, the phantom bit is set as $m = 4$, and the ratio of the element spacing to the radar wavelength is $d/\lambda = 0.5$. The real detector dislocation angle can be calculated according to the model given in Appendix B.

The missile motion and LOS angle input are modeled with a sinusoidal signal:

$$\begin{cases} \dot{\psi} = 20\sin(2\pi f_{\mathrm{m}}t) \\ \dot{\vartheta} = 20\sin(2\pi f_{\mathrm{m}}t) \\ \dot{\gamma} = 0 \end{cases} \quad \begin{cases} \dot{q}_y = 2\sin(0.3t + \pi/2) \\ \dot{q}_z = 3\sin(0.3t) \end{cases}$$

where $\dot{\psi}, \dot{\vartheta}, \dot{\gamma}$ are the missile body attitude rates and f_{m} is the varying frequency of the missile attitude rate. The LOS angle rate inputs are set as $\dot{q}_y$ and $\dot{q}_z$ without considering the missile body roll.

Four processing conditions are used to simulate the LOS rate extraction performance of PARS when the disturbance frequency of the missile is set as $f_{\mathrm{m}} = 2$ Hz, which are shown in Figs. 14–17. The forward path detector gain is set as $k = 10$. The actual LOS rate input is projected to the beam-pointing coordinate system, and the LOS rate outputs from the LOS rate extraction model for the two channels are compared. Thereafter, the decoupling effect is analyzed. In the simulation, the decoupling effect can be expressed with the decoupling coefficient (η) as follows:

$$\eta = \left|\frac{\text{LOS rate maximum error estimation value}}{\text{Body motion maximum}}\right|$$

Processing condition 1: Without considering noise input

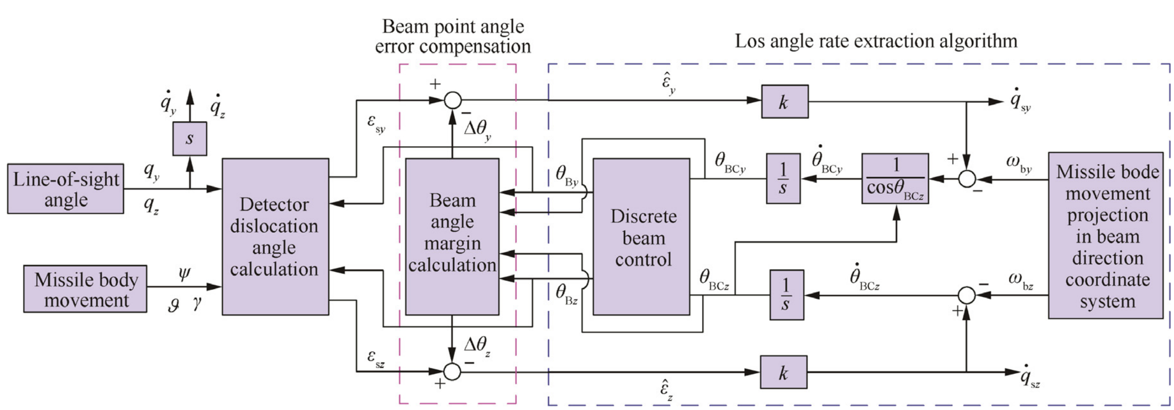

Fig. 13 LOS rate extraction model for two channels used for BPT.

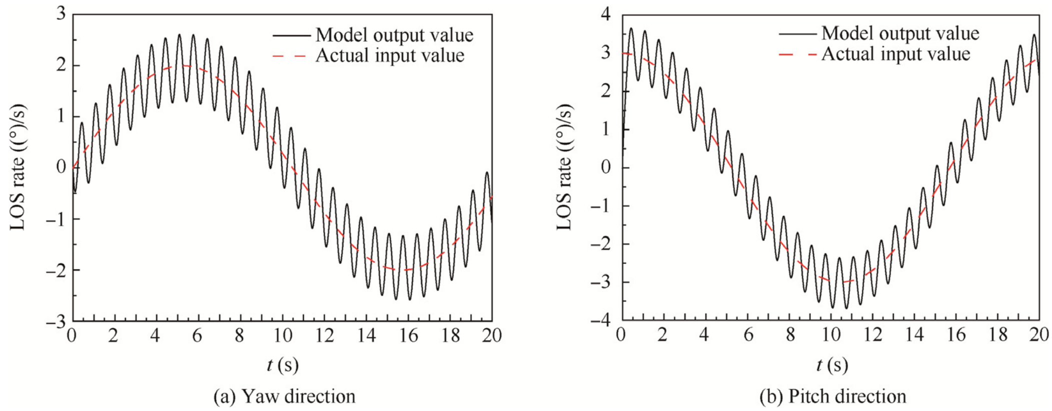

Fig. 14 LOS rate comparison diagram without considering noise input.

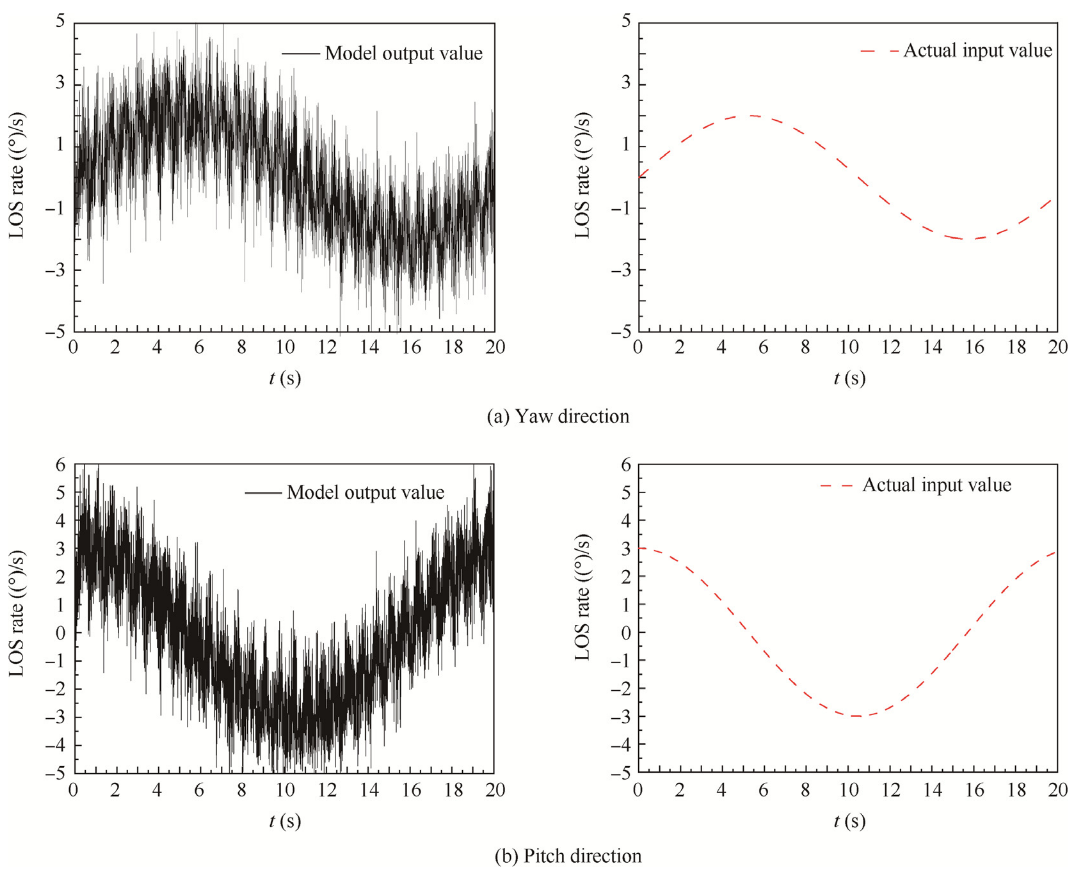

Fig. 15 LOS rate comparison diagram considering noise input.

Fig. 14(a) and (b) show the LOS rate comparison diagram in the pitch and yaw directions by only considering the beam-pointing error.

Processing condition 2: Considering noise input

Based on Condition 1, the variance is 0.012 by adding the zero mean WGN noise at the beam-pointing angle output point. Fig. 15(a) and (b) show the LOS rate comparison diagram in the pitch and yaw directions by considering the noise input.

Processing condition 3: Adopting a low-pass filter

A low-pass filter is added at the LOS rate extraction point. Fig. 16(a) and (b) show that the LOS rate comparison diagram in the pitch and yaw directions adopts the low-pass filter.

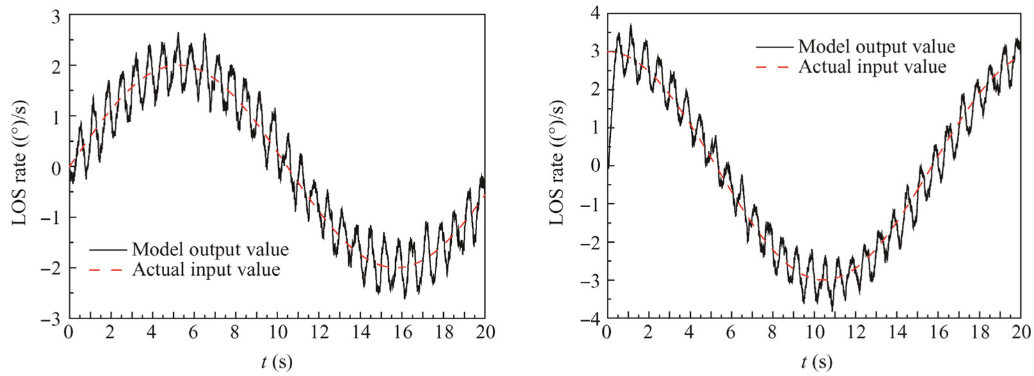

(a) Yaw direction (b) Pitch direction

Fig. 16 LOS rate comparison diagram with a low-pass filter.

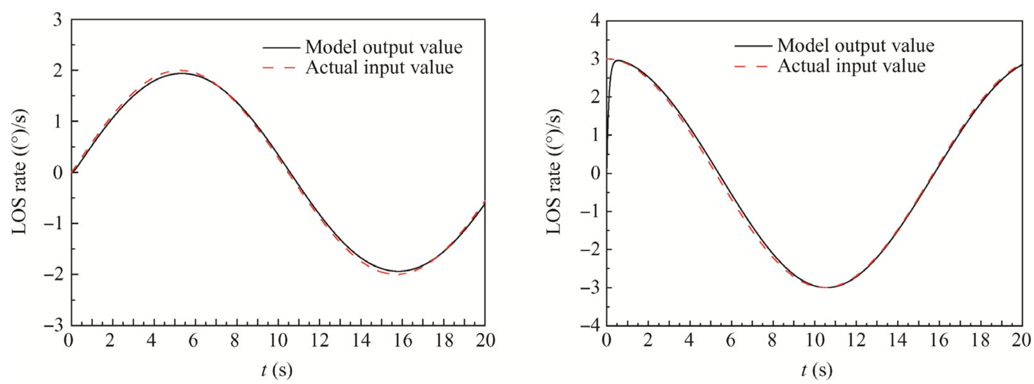

(a) Yaw direction (b) Pitch direction

Fig. 17 LOS rate comparison diagram with beam-pointing angle error compensation.

Table 2 Maximum error estimation value of LOS rate and decoupling factor for four conditions.

Frequency of missile (Hz)	Processing condition	Body motion maximum ((°)/s)		LOS rate maximum error estimation value ((°)/s)		Decoupling factor	
		y-axis	*z*-axis	*y*-axis	*z*-axis	*y*-axis	*z*-axis
1	Condition 1	20	20	0.63	0.96	3.15%	4.8%
	Condition 2	–	–	2.85	4.28	14.25%	21.4%
	Condition 3	–	–	0.56	0.82	2.8%	4.1%
	Condition 4	–	–	0.104	0.112	0.52%	0.56%
1.5	Condition 1	–	–	0.66	0.84	3.3%	4.2%
	Condition 2	–	–	2.87	4.64	14.35%	23.2%
	Condition 3	–	–	0.525	0.81	2.63%	4.05%
	Condition 4	–	–	0.127	0.144	0.635%	0.072%
2	Condition 1	–	–	0.93	0.98	4.65%	4.95%
	Condition 2	–	–	2.41	4.16	12.05%	20.8%
	Condition 3	–	–	0.71	0.85	3.55%	4.25%
	Condition 4	–	–	0.145	0.152	0.725%	0.76%
3	Condition 1	–	–	1.14	1.27	5.7%	6.35%
	Condition 2	–	–	2.45	4.0	12.25%	20.0%
	Condition 3	–	–	0.578	0.93	2.89%	4.65%
	Condition 4	–	–	0.167	0.172	0.835%	0.86%
4	Condition 1	–	–	0.63	0.87	3.15%	4.35%
	Condition 2	–	–	2.44	4.28	12.2%	21.4%
	Condition 3	–	–	0.445	0.67	2.22%	3.35%
	Condition 4	–	–	0.205	0.214	1.02%	1.07%

Processing condition 4: Use of beam-pointing angle error compensation

Fig. 17(a) and (b) show the LOS rate comparison diagram in the pitch and yaw directions with beam-pointing angle error compensation.

Fig. 14 illustrates that the LOS rate extraction value presents a fluctuation phenomenon because of the beam-pointing error in the beam control process. It can be found from Fig. 15 that discrete beam scanning results in beam-pointing angle error and causes a PARS disturbance rejection rate parasitical effect, which leads to severe noise amplification and severe LOS rate output fluctuations. Although the LOS rate performance is improved when the low-pass filter process is adopted (Fig. 16), fluctuations still exist. From Fig. 17, the LOS rate performance is significantly improved with the beam-pointing angle error compensation method. The estimated LOS rate follows the actual LOS rate input value smoothly and accurately. Table 2 shows the maximum error estimation value of the LOS rate and the decoupling factor for the four conditions at different disturbance frequencies of the missile; the y-axis and z-axis express the pitch and yaw directions, respectively, the maximum error estimation value of the LOS rate in Condition 4 is lower than that in Conditions 1, 2, and 3, and the decoupling factor is small in Condition 4. The beam-pointing error compensation can effectively isolate the body motion and accurately extract the LOS rate. At the same time, the larger the disturbance frequency of the missile is, the larger the decoupling factor is.

The effects of PBT on the LOS rate and LOS angle outputs are shown in Table 3; the phantom bit m is set to 2, 3, 4 and 5, and the forward path gain k = 10. From the simulation results, we can easily see that the larger m is, the larger the LOS angle tracking error and LOS rate estimation error are.

Table 3 Error change situation with different values of m.

Phantom bit m	LOS angle tracking error (°)		LOS rate maximum error estimation value ((°)/s)	
	y-axis	z-axis	y-axis	z-axis
2	0.0034	0.0062	0.13	0.19
3	0.05	0.048	0.28	0.24
4	0.17	0.25	0.93	0.98
5	0.84	0.92	1.85	1.93

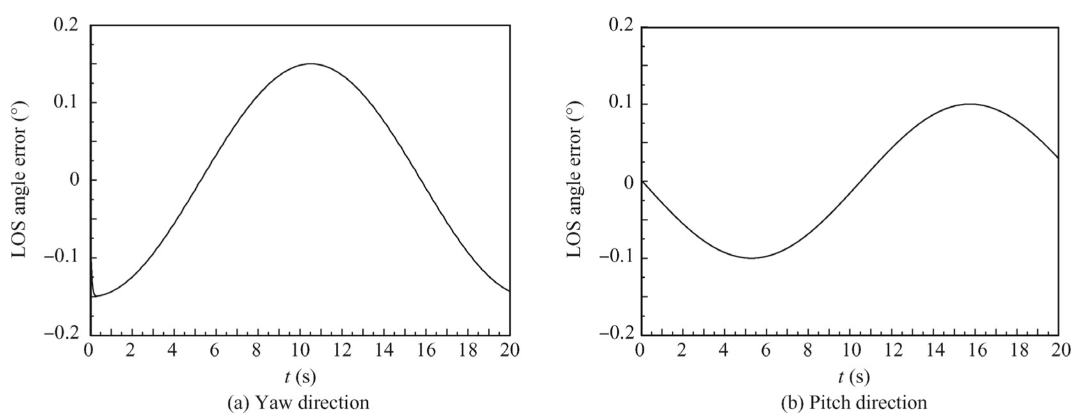

Fig. 18 LOS angle tracking error curve (k = 20).

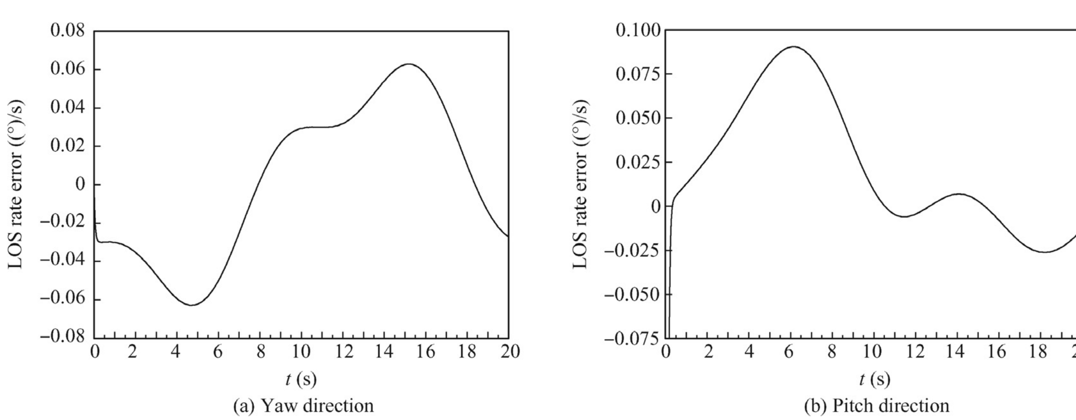

Fig. 19 LOS rate error curve (k = 20).

Table 4 Error change situation with different values of k.

Gain k	LOS angle tracking error (°)		LOS rate maximum error estimation value ((°)/s)	
	y-axis	z-axis	y-axis	z-axis
10	0.30	0.28	0.145	0.152
20	0.15	0.10	0.063	0.085
30	0.10	0.09	0.054	0.062
40	0.071	0.075	0.043	0.05

Second, we use the beam control model (Fig. 14) to simulate the effects of the forward path detector gain (k) on the LOS rate and LOS angle outputs. The forward path gain k and R_i are set to 20 and 0, respectively. The simulation results of Figs. 18 and 19 show that the LOS angle tracking errors are close to 0.15° and 0.1° in the yaw and pitch directions, respectively. The LOS rate estimation error reaches 0.063 (°)/s and 0.85 (°)/s in the yaw and pitch directions, respectively. From Table 4, we can note that the larger k is, the smaller the error is. One reason is that the larger k can reduce the delay time, increasing the tracking loop rapidly.

5. Conclusions

(1) The difference between the theoretical phase shift value and virtual phase shift value with PBT will lead to beam-pointing error, which is related to the number of phantom bits. The greater m is, the greater the beam-pointing error envelope is. The beam-pointing error increases with the beam scan angle and then causes BPES. As a result, body movements are coupled to the LOS rate output, which affects the accuracy of the LOS rate and stability margin of the guidance system.

(2) A two-channel decoupling algorithm and an LOS rate extraction model with the BPE compensation method for PARS are proposed. The beam angle margin in the pitch and yaw directions was calculated to reduce the effect of the missile body disturbance and to improve LOS rate extraction precision by compensating for the detector dislocation angle. The simulation results show that the LOS rate maximum error estimation value in Condition 4 is considerably lower than that in Conditions 1, 2 and 3. The decoupling factor is considerably smaller in Condition 4. BPE compensation could effectively isolate the body motion, and the LOS rate could be extracted accurately.

(3) The larger the phantom bit (m) is, the larger the LOS angle tracking error and LOS rate estimation error are. At the same time, the forward path detector gain (k) also affects the tracking performance of PARS; the larger k is, the smaller the error is. In summary, use of the proposed BPE compensation method could improve the LOS rate extraction precision, thereby enhancing the missile guidance precision.

Appendix A

The coordinate systems used in this study are defined as follows:

(1) Inertial coordinate system (S_i) $Ox_\mathrm{i}y_\mathrm{i}z_\mathrm{i}$

The x_i-axis points to random direction, and the y_i-axis points along the vertical direction. The z_i-axis direction can be obtained by the right-hand rule.

(2) Missile body coordinate system (S_m) $Ox_\mathrm{m}y_\mathrm{m}z_\mathrm{m}$

The x_m-axis coincides with the lengthwise axis of the missile and points to the front of the missile. The y_m-axis is located within the missile longitudinal symmetry plane and is perpendicular to the x_m-axis. The z_m-axis direction can be obtained by the right-hand rule.

(3) LOS coordinate system (S_l) $Ox_\mathrm{l}y_\mathrm{l}z_\mathrm{l}$

The x_l-axis points to the target. The y_l-axis is located within the vertical plane that contains the x_l-axis and is perpendicular to the x_l-axis. The z_l-axis direction can be obtained by the right-hand rule.

(4) Beam-pointing coordinate system (S_b) $Ox_\mathrm{b}y_\mathrm{b}z_\mathrm{b}$

The x_b-axis points to the beam center axis. The y_b-axis is located within the plane that contains the x_b-axis and is perpendicular to $Ox_\mathrm{m}z_\mathrm{m}$ plane. The y_m axis is perpendicular to x_m. The z_b-axis direction can be obtained by the right-hand rule.

(5) Virtual beam-pointing coordinate system ($S_{\hat{\mathrm{b}}}$) $Ox_{\hat{\mathrm{b}}}y_{\hat{\mathrm{b}}}z_{\hat{\mathrm{b}}}$

The $x_{\hat{\mathrm{b}}}$-axis points to the direction defined by beam angle instruction. The $y_{\hat{\mathrm{b}}}$-axis is located within the plane that contains the $x_{\hat{\mathrm{b}}}$-axis and is perpendicular to the $Ox_\mathrm{m}z_\mathrm{m}$ plane. The $y_{\hat{\mathrm{b}}}$-axis is perpendicular to $x_{\hat{\mathrm{b}}}$. $z_{\hat{\mathrm{b}}}$-axis direction can be obtained with the right-hand rule.

(6) Measurement coordinate system (S_c) $Ox_\mathrm{c}y_\mathrm{c}z_\mathrm{c}$

The x_c-axis points to the target. The y_c-axis is located within the plane that contains the x_c-axis and is also perpendicular to the $Ox_\mathrm{b}z_\mathrm{b}$ plane. y_c-axis is perpendicular to x_c. The z_c-axis direction can be obtained by the right-hand rule.

According to the definition of coordinates, Fig. A1 shows the coordinate transform relationship.

In Fig. A1, ψ, ϑ and γ denote the missile body yaw angle, pitch angle and roll angle, respectively, with S_i as a benchmark; q_{sy} and q_{sz} are the LOS angles in the yaw and pitch directions, respectively, with S_i as a benchmark; $\theta_{\mathrm{BC}y}$ and $\theta_{\mathrm{BC}z}$ are the beam-pointing angles in the yaw and pitch

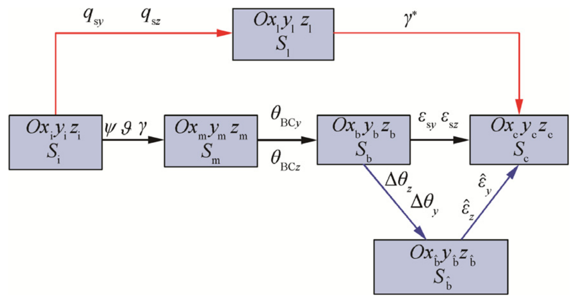

Fig. A1 Transformation of coordinate systems.

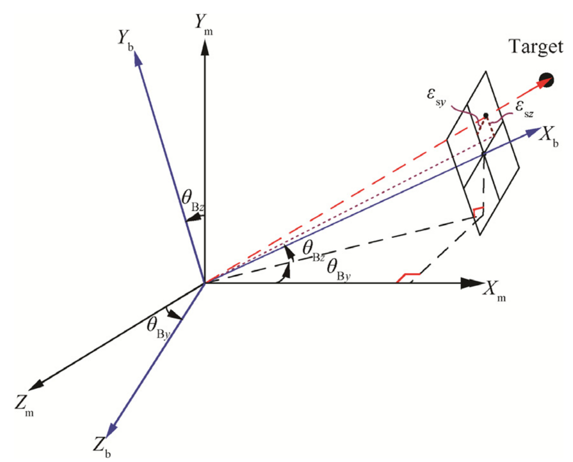

Fig. B1 Geometric relationship for practical detector dislocation angle calculation.

directions, respectively, with S_b as a benchmark; ε_{sy} and ε_{sz} are the seeker detector dislocation angles in the yaw and pitch directions, respectively, with S_b as a benchmark; $\Delta\theta_y$ and $\Delta\theta_z$ are the angle deviations from S_b to $S_{\hat{b}}$ in the yaw and pitch directions, respectively, with $S_{\hat{b}}$ as a benchmark; $\hat{\varepsilon}_y$ and $\hat{\varepsilon}_z$ are the angle deviations from S_l to $S_{\hat{b}}$ in the yaw and pitch directions, respectively, with $S_{\hat{b}}$ as a benchmark.

Appendix B

Fig. B1 shows the geometric relationship for practical detector dislocation angle calculation. The unit vector is supposedly $\boldsymbol{a}^{\hat{b}} = [1, 0, 0]^{\mathrm{T}}$ in the LOS coordinate system, which can be projected to $S_{\hat{b}}$ and is denoted as $[x_{sb}, y_{sb}, z_{sb}]^{\mathrm{T}}$.

$$[x_{sb}, y_{sb}, z_{sb}]^{\mathrm{T}} = \boldsymbol{C}_{mb}\boldsymbol{C}_{im}\boldsymbol{C}_{li}\boldsymbol{i}$$

where

$$\boldsymbol{C}_{li} = \boldsymbol{C}_{il}^{-1} = \begin{bmatrix} \cos q_y \cos q_z & -\cos q_y \sin q_z & \sin q_y \\ \sin q_z & \cos q_z & 0 \\ -\sin q_y \cos q_z & \sin q_y \sin q_z & \cos q_y \end{bmatrix}$$

$$\boldsymbol{C}_{im} = \begin{bmatrix} \cos\vartheta\cos\psi & \sin\vartheta & -\cos\vartheta\sin\psi \\ -\sin\vartheta\cos\psi\cos\gamma + \sin\psi\sin\gamma & \cos\vartheta\cos\gamma & \sin\vartheta\sin\psi\cos\gamma + \cos\psi\sin\gamma \\ \sin\vartheta\cos\psi\sin\gamma + \sin\psi\cos\gamma & -\cos\vartheta\sin\gamma & -\sin\vartheta\sin\psi\sin\gamma + \cos\psi\cos\gamma \end{bmatrix}$$

$$\boldsymbol{C}_{mb} = \begin{bmatrix} \cos\theta_{By}\cos\theta_{Bz} & \sin\theta_{Bz} & -\sin\theta_{By}\cos\theta_{Bz} \\ -\cos\theta_{By}\sin\theta_{Bz} & \cos\theta_{Bz} & \sin\theta_{By}\sin\theta_{Bz} \\ \sin\theta_{By} & 0 & \cos\theta_{By} \end{bmatrix}$$

The detector dislocation angle calculation formula is expressed as follows:

$$\begin{cases} \varepsilon_{sy} = \arctan\left(-\frac{z_{sb}}{x_{sb}}\right) \\ \varepsilon_{sz} = \arctan\left(\frac{y_{sb}}{x_{sb}}\right) \end{cases}$$

The PARS output is obtained by the beam-pointing angle error compensation, which can be expressed as follows:

$$\begin{cases} \hat{\varepsilon}_y = \varepsilon_{sy} - \Delta\theta_y \\ \hat{\varepsilon}_z = \varepsilon_{sz} - \Delta\theta_z \end{cases}$$

References

1. Fan HT, Yang J, Zhu XP. Research on beam stabilization technology of phased array radar seeker. *Acta Aeronaut Astronaut Sinica* 2013;**34**(2):387–92 [Chinese].
2. Janice CR, James HM, Joel PB, Hudson T. The past, present, and future of electronically-steerable phased arrays in defense applications. *Proceedings of aerospace conference*; 2008 Mar 1–8; 2008. p. 1–7.
3. Mailloux RJ. *Phased array antenna handbook*. 2nd ed. Boston: Artech House; 2005.
4. Garrod A. Digital modules for phased array radar. *IEEE international symposium on phased array systems and technology*; 1996 Oct 15–18; 1996. p. 81–6.
5. Hord WE, Boyd CR, Diaz D. A new type of fast switching dual-mode ferrite phase shifter. *IEEE Trans Microwave Theory Tech* 1988;**35**(12):985–8.
6. Davis ME. Integrated diode phase-shifter elements for an X-band phased-array antenna. *IEEE Trans Microwave Theory Tech* 1975;**23**(12):1080–4.
7. Jang SA, Ryoo CK, Choi K, Tahk MJ. Guidance algorithms for tactical missiles with strapdown seeker. *SICE annual conference*; 2008 Aug 20–22; 2008. p. 2616–9.
8. Savage PG. Strapdown sculling algorithm design for sensor dynamic amplitude and phase-shift error. *J Guid Control Dyn* 2012;**35**(6):1718–29.
9. Lu TY, Wen QQ, Yin J. The effect of phantom-bit technology on the performance of phased array seeker detection in the case of the initial beam angle. *Optik-Int J Light Electron Opt* 2016;**127**(20):9996–10003.
10. Zarchan P. *Tactical and strategic missile guidance*. 6th ed. Reston: American Institute of Aeronautics & Astronautics; 1990. p. 555.
11. Du X, Xia QL. The research of guidance performance of the phased array seeker with platform for air-to-air missile. *Optik-Int J Light Electron Opt* 2016;**127**(22):10322–34.
12. Song J, Wang J, Peng K, Pan C, Yang Z. Quantization error reduction for the phased array with 2-bit phase shifter. *Wirel Personal Commun* 2010;**52**(1):29–41.
13. Smith MS, Guo YC. A comparison of methods for randomizing phase quantization errors in phased arrays. *IEEE Trans Anten Propag* 1983;**31**(6):821–8.
14. Guan BR, Chen XH. A phased-array antenna for terrestrial satellite communication based on vitual phase shifting. *J Microwaves* 2011;**27**(4):45–8 [Chinese].
15. Nesline FW, Zarchan P. Radome induced miss distance in aerodynamically controlled homing missiles. *17th fluid dynamics, plasma dynamics, and lasers conference*; 1984. p. 99–115.

16. Du YL, Xia QL, Cai CT. Study on miss-distance of radar seeker guided missile due to radome slope error. *J Project Rock Missiles Guidance* 2010;**30**(5):79–82 [Chinese].
17. Song T, Lin DF, Wang J. Influence of seeker disturbance rejection rate on missile guidance system. *J Harbin Eng Univ* 2013;**34**(10):1234–41 [Chinese].
18. Li FG, Xia QL, Qi ZK, Sun J. Effect of parasitic loop on strap-down seeker and compensated with identification method. *Syst Eng Electron* 2013;**35**(8):1717–22 [Chinese].
19. Peterson D, Otto J, Douglas K. Radome boresight error and compensation techniques for electronically scanned arrays. *Annual interceptor technology conference*; 1993.